Chapter 4

Radiation Power and Electrode Detachment

This chapter reports the experimental results of the vacuum photodiode array described in Chapter 3. The sheer size of the vacuum photodiode signals implies large levels of radiative power coming from the plasma and has important implications regarding the plasma temperature and ionization balance. These radiation levels are estimated in Sec. 4.1.1 and compared to the rate of Ohmic dissipation in Sec. 4.1.2, where it is proposed that a large majority of the heat deposited by Ohmic dissipation is emitted as extreme ultraviolet (EUV) radiation. Possible mechanisms for the EUV radiation are then discussed in Sec. 4.1.3 and Sec. 4.1.4. Section 4.2 compares the EUV emission levels between co- and counter-helicity plasma. As anticipated from Hansen et al. [20], counter-helicity plasmas emit large bursts of radiation that are not seen in their co-helicity counterparts. A new finding, however, is that the locations of these bursts depends on the amount of neutral gas injected into the chamber. In Sec. 4.3, we shall explore how the charging voltage of the fast gas valve capacitor bank, discussed in Sec. 2.1.2, influences the vacuum photodiode signals as well as other diagnostic data.

4.1 Radiative Losses, Ohmic Heating, and Line Emission

The vacuum photodiodes register signals on the order of a tenth of a volt and higher, depending on the plasma parameters. These signals, obtained without amplification, suggest very high radiation levels that appear consistent with the theory that low-temperature plasmas radiate away any heat deposited by Ohmic dissipation, as will be discussed in Sec. 4.1.2. The exact cause of the vacuum photodiode signals has not been identified, but the chief suspect is presently hydrogen line emission as opposed to impurity radiation or thermal bremsstrahlung.

4.1.1 Vacuum Photodiode Power Flux

From the magnitude of the vacuum photodiode signals, we can roughly estimate the radiation intensity incident on a vacuum photodiode as well as the total power radiated by a hydrogen plasma. This estimate suggests that the plasma radiates megawatts of power. The vacuum photodiode output current is equivalent to the number of electrons photoemitted per second and equals the vacuum photodiode output voltage divided by 50 Ω. To estimate the number of incident photons required to emit these electrons, we assume that the vacuum photodiode signals are entirely due to the hydrogen Lyman α ($\mathrm{H}_{\mathrm{L}\alpha}$)[1] line, which we expect to be the dominant line emission. The error incurred by this assumption will be discussed below. $\mathrm{H}_{\mathrm{L}\alpha}$ photons have an energy of 10.2 eV and a wavelength of 121.6 nm; the yield of an aluminum cathode at 121.6 nm is approximately 0.038 electrons per photon (e^-/γ) as given by Fig. 3.2. It follows that the power incident on a single diode is

$$P_{\text{diode}} = \frac{V_{\text{diode}}}{50\ \Omega} \cdot \frac{1}{1.6 \cdot 10^{-19}\ \mathrm{C/e^-}} \cdot \frac{1}{0.038\ \mathrm{e^-}/\gamma} \cdot 10.2\ \frac{\mathrm{eV}}{\gamma} = (5\ \mathrm{W/V}) \cdot V_{\text{diode}}, \tag{4.1}$$

where V_{diode} is the vacuum photodiode output voltage.

P_{diode} is the power incident on the diode, which is only a fraction of the power radiated in all directions by the plasma. To estimate this latter quantity, we regard the plasma as a sheet of uniformly emitting material as in Sec. 3.5.3 and compute the power radiated per unit area, σ, using Eq. (3.10), which we reproduce here after setting $\alpha = 0$:

$$\sigma = \frac{4\pi\rho^2 P_{\text{diode}}}{A_{\text{diode}} A_e^*}. \tag{4.2}$$

Note that each vacuum photodiode monitors a total area $A_0 = 69\ \mathrm{cm}^2$, but we use the *effective* area A_e^* in Eq. (3.10) to account for the shadowing effects of the collimator. As given by Table 3.2, $A_e^* = 2.6\ \mathrm{cm}^2$ at the midpoint of the electrodes. ρ is the distance from the back of the collimator to the midpoint of the electrodes, so $\rho = 37$ cm, while A_{diode} is the cross-sectional area of the collimator, so $A_{\text{diode}} = 0.45\ \mathrm{cm}^2$. Given σ, we extrapolate the total plasma emission by multiplying σ by the *total* area A_0 monitored by a vacuum photodiode:

$$P = \sigma A_0 = P_{\text{diode}} \frac{4\pi\rho^2}{A_{\text{diode}}} \frac{A_0}{A_e^*} = \left(1 \cdot 10^6\right) \cdot P_{\text{diode}}. \tag{4.3}$$

We emphasize that the factor A_0/A_e^* is due to the collimation of the detectors and is only accurate to the degree to which the plasma uniformly emits over the vacuum photodiode field of view. Equation (4.3) says that, if a vacuum photodiode reads 0.1 V, then the corresponding area of the plasma is radiating about 0.5 MW.

---

[1] We adopt the following notation for hydrogen lines: the Balmer lines will be denoted as H_α and H_β while the Lyman lines will be denoted $\mathrm{H}_{\mathrm{L}\alpha}$ and $\mathrm{H}_{\mathrm{L}\beta}$.

Of course, the accuracy of Eqs. (4.1) and (4.3) depends on several assumptions. We assumed that the radiation was monochromatic at the $\mathrm{H}_{\mathrm{L}\alpha}$ line; we will explain the rational for assuming that hydrogen emission is dominant in Sec. 4.1.3. We now explore how the estimated power changes with assumed wavelength. If we assume a photon energy of 13.6 eV, where the photoyield of an aluminum cathode peaks at 0.19 e^{-}/γ, we obtain a vacuum photodiode power of 1.4 W/V. If we instead assume photons at 30 nm, near the low-wavelength limit of an aluminum cathode where the yield is roughly 0.05 e^{-}/γ, we obtain a vacuum photodiode power of 16 W/V. Thus, our assumption of monochromatic $\mathrm{H}_{\mathrm{L}\alpha}$ radiation is at worst incorrect by a factor of three. This should be compared to the uncertainty of $\pm$ 30% in the yield of a metallic cathode in typical laboratory conditions [59]. Finally, we also assumed that the plasma emits homogenously over the detector viewing area, which leads to the factor of A_0/A_e^* in Eq. (4.3). However, the exact degree to which the collimator shadows the vacuum photodiode from the plasma radiation depends on how the radiation is distributed within the vacuum photodiode field of view. For instance, if all the radiation originates from a point source at the center of the detector's viewing area, then the collimation has no shadowing effect on the signal, and the factor A_e^*/A_0 would be inaccurate. Nonetheless, we expect Eqs. (4.1) and (4.3) to hold to within an order of magnitude, and we see that vacuum photodiode signals on the order of a volt correspond to megawatts of radiation power.

4.1.2 Ohmic Heating and Radiative Losses

Simple calculations suggest that Ohmic dissipation of the plasma current should steadily heat the plasma to higher and higher temperatures if no mechanism exists to carry away this energy. Such heating is not observed in the Caltech experiments, for a plasma made of argon or nitrogen that is steadily heated from 1 eV to 10 eV would rapidly progress through its ionization states, and this behavior is not observed. Instead, radiative losses, primarily in the EUV, carry away the Ohmic heat, and we investigate this possibility by comparing the radiation estimates of the previous section to estimates of Ohmic dissipation. Although the figures reported here are only accurate to within an order of magnitude, it seems plausible that the Ohmic heat is indeed lost to EUV radiation.

To quantify the issue of Ohmic heating, we compute the theoretical rate of increase of temperature assuming the energy of Ohmic dissipation ends up as thermal particle energy with no loss of energy as radiation. The thermal energy is $(3/2)k_BT$ per particle, so for a singly ionized plasma we sum over electrons and ions to get a thermal energy density of $3k_BTn$, where we have assumed that electrons and ions share that same temperature. We take $n \sim 10^{21}$ m^{-3} based on Stark broadening measurements of the H_β lines as discussed in Sec. 2.2.4. This thermal energy density is fueled by Ohmic dissipation, whose power density is $\mathbf{E}\cdot\mathbf{J} = \eta J^2 = \eta I^2/A_c^2$, where η is the plasma resistivity, I is the plasma current, and A_c is the cross-sectional area of the plasma loop. If all of the energy of

Ohmic dissipation goes into thermal energy, then

$$\dot{T} = \frac{2\eta I^2}{3A_c^2 n k_B}. \tag{4.4}$$

From fast camera images, the radius of the plasma loop is approximately 2 cm. The plasma resistivity will be estimated using Fokker-Planck theory [2, pg. 451]:

$$\begin{aligned} \eta &= \frac{Ze^2\sqrt{m_e}\ln\Lambda}{3\pi^{3/2}\epsilon_0^2(2k_BT_e)^{3/2}} && (4.5) \\ &= 1.03\cdot 10^{-4}\frac{Z\ln\Lambda}{T_e^{3/2}}, && (4.6) \end{aligned}$$

where $\ln\Lambda$ is the usual Coulomb logarithm [75, pg. 34]. Using $Z = 1$, $\ln\Lambda = 7$, and $T_e = 3$ eV gives $\eta = 1.4\cdot 10^{-4}$ Ωm. Therefore, at a modest current of 10 kA, we would have $\dot{T} \sim 20$ eV/μs. Clearly, under such conditions the plasma would rapidly heat up to very high temperatures, which is not observed experimentally. This indicates that radiative losses must be transporting energy out of the plasma at a rate comparable to the Ohmic dissipation.

To estimate the total amount of heat generated in the plasma loop, we model the plasma as a uniform cylinder of radius r, length l, and resistivity η, from which the plasma resistance is $R_p = \eta l/(\pi r^2)$. We take $r = 2$ cm and $l = 20$ cm, which gives an estimated resistance of the plasma cylinder of 20 mΩ. This is only a rough estimate. The length of the loop grows steadily throughout the course of a shot due not only to the overall expansion but also due to the kinking of the flux tube. The loop radius is not always clearly defined from the camera images. Moreover, the current may not flow entirely through the loop in fast camera images. On the Spheromak experiment, magnetic data indicate that the current flows in a radius over three times larger than the radius seen in camera images [37]. If this is also true for the Solar Loop Experiment, the plasma resistance and Ohmic dissipation would be smaller be a factor of nine. Also, on the Solar Experiment, current still flows between the electrodes even at late times when Imacon images suggest that the plasma has detached from the electrodes. It is not clear where the current flows at this point; it may partially flow through arcs observed between and behind the electrodes. Finally, we note that Z, which should be averaged over all ions, both majority and impurity, may have a bigger value than $Z = 1$ depending on the impurity concentration. Thus, there are several factors that make our estimate of 20 mΩ accurate only to within an order of magnitude.

Radiative losses in the EUV appear to balance Ohmic dissipation. Figure 4.1 plots both these quantities for a single-loop hydrogen plasma formed with a 5 kV discharge (shot 8959). The UV radiation power is obtained by summing all twelve vacuum photodiode signals and applying the conversion factors in Eqs. (4.1) and (4.3). The Ohmic heating power is given as $R_pI(t)^2$ with R_p estimated above as 20 mΩ. The two power levels are close in magnitude; moreover, the shapes of the two traces are especially similar during the first three microseconds. Both the estimates for Ohmic dissipation and UV emission are rough, and at this level of accuracy it appears very possible that the UV radiation indeed balances the Ohmic dissipation. We note that the vacuum photodiode array does not view the entire plasma, and thus the UV power computed here is smaller than the total UV power. Plans are in place to install another set of vacuum photodiodes whose field of view will cover the entire plasma and whose signal will thus reflect the total UV emission. These vacuum photodiodes will also have reduced uncertainties in regards to computing the total power radiated because they will not be significantly collimated, and the factor of A_0/A_e^* in Eq. (4.3) will very close to unity.

We can compare the power levels of EUV radiation and Ohmic dissipation to other power levels in the experiment. Figure 4.1 plots the total input power $P_{\text{tot}} = I(t)V(t)$, where V is the electrode voltage. The total input power is an order of magnitude larger than both the UV emission and Ohmic heating, and the rapid decline of the input power corresponds to the voltage going to zero and changing sign. We thus see that while radiative losses are significant, they do not dominate the energy budget, and there is ample energy available for the plasma kinetic and magnetic energy. Figure 4.1 also plots an estimate of the optical power as estimated from an optical photodiode, as will be discussed below. While the optical power is over an order of magnitude smaller than the UV emission, its curve has roughly the same shape during the first several microseconds.

By varying the discharge voltage of the main bank, the UV radiation is seen to be determined by the instantaneous value of the plasma current. In Fig. 4.2.a, the vacuum photodiode signal is plotted as a function of time for different discharge voltages. For larger discharge voltages, the vacuum photodiode signal rises more rapidly in the first several microseconds. In Fig. 4.2.b, however, the vacuum photodiode signals are instead plotted as a function of current and are seen to coincide with each other during early times. During this phase, the UV radiation depends only on the instantaneous value of the current. Moreover, this dependence is roughly quadratic, and fitting the UV power levels with the square of the current gives a plasma resistance of 5.3 mΩ. At a certain point in time, however, the UV signal diverges from this quadratic dependence on current; this occurs at earlier times for lower discharge voltages. The reason from this departure from the quadratic behavior is not yet understood and presents an intriguing possibility for future research.

Also shown in Figs. 4.2.c and 4.2.d are estimates of the optical radiation obtained from optical-photodiode data. A PDA36A photodiode by ThorLabs[2] was mounted on a viewport looking across the vacuum vessel at the electrodes. The advantage of this positioning was that the field of view of the optical photodiode covered the entire plasma, unlike the collimated vacuum photodiodes. For hydrogen plasmas, we assume that the photodiode signals comes entirely from the Balmer α (656

---

[2] The author graciously acknowledges Matthew Kelley for suggesting this diode and lending one to the lab.

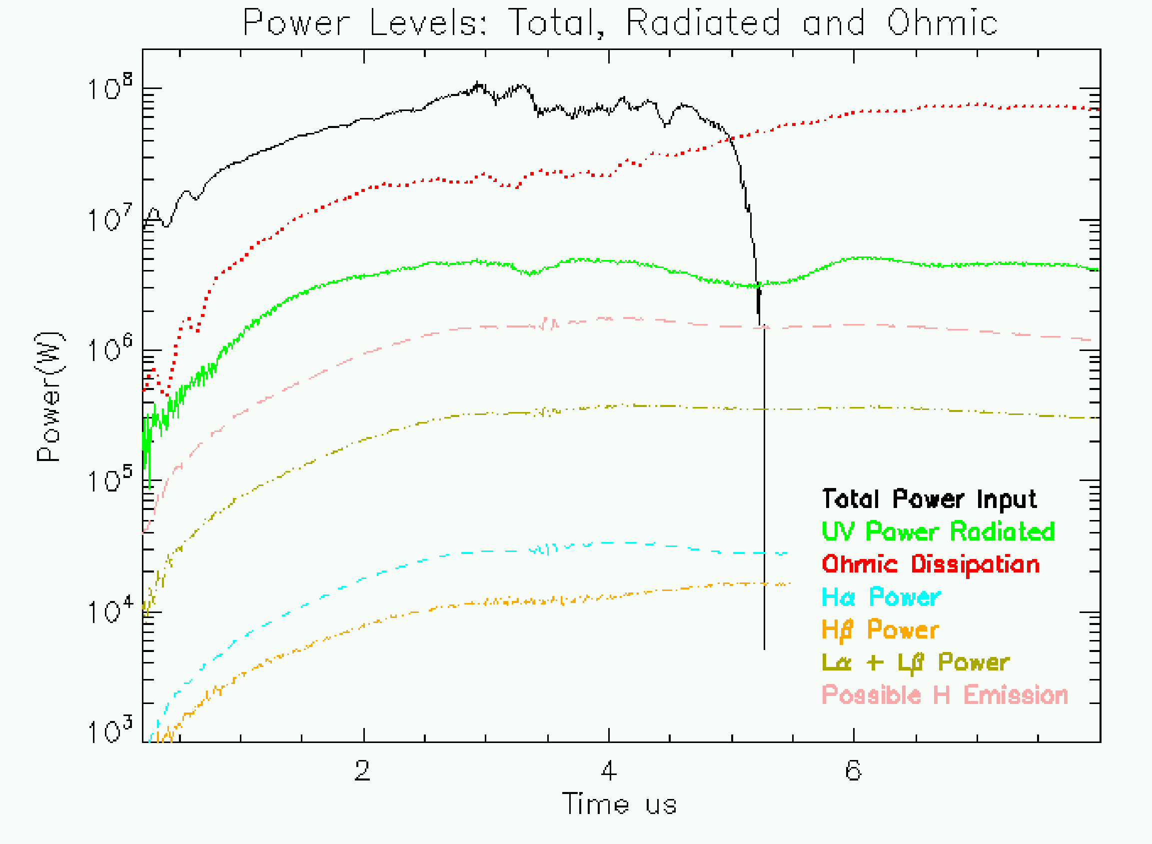

Figure 4.1: A plot of various power levels: the total input power, the estimate for Ohmic dissipation, the total EUV radiative losses, radiative losses from the optical H_α and H_β lines, the associated power loss from the $H_{L\beta}$ and $H_{L\gamma}$ lines, and an estimate for the total hydrogen emission.

nm) line, for which the diode responsivity is 0.408 A/W [76]. Thus,

$$P_{\text{diode}} \approx \frac{V_{\text{diode}}}{50\ \Omega \cdot 0.408\ \text{A/W}}. \tag{4.7}$$

The optical photodiode does not have any collimation, so we use Eq. (3.5) to estimate the total optical power radiated,

$$\begin{aligned} P_{\text{optical}} &= P_{\text{diode}} \cdot \frac{4\pi\rho^2}{A_{\text{diode}}} && (4.8)\\ &= (120,000\ \text{W/V}) \cdot V_{\text{diode}}, && (4.9) \end{aligned}$$

where the optical photodiode area is 13 mm^2 and $\rho = 1.58$ m is the separation between the optical photodiode and the electrodes. It is possible that reflections of visible light rays within the chamber can make Eq. (4.9) overestimate the true optical power, but we do not expect reflections to be especially significant based on fast camera images. As shown in Fig. 4.1, the power radiated in the optical domain is much smaller than both the UV power and the Ohmic dissipation. However, as is seen in Fig. 4.2.c, the optical signals follow the same trend as the vacuum photodiode signals for early times and, when plotted as a function of current, coincide with each other, confirming that radiation at different discharge voltages is indeed a function of the instantaneous current.

The data in Fig. 4.2 were taken holding the charging voltage of the fast gas valve capacitor bank fixed so that the amount of neutral gas available to the plasma is fixed (see Sec. 2.1.2). If the charging voltage is varied, then the traces do not overlap as well even if the discharge voltage is held fixed. We hypothesize that the different charging voltages for the fast gas valve capacitor bank induce different plasma densities that change the emissivity of the plasma, as will be discussed in the next section.

In conclusion, the magnitude of the EUV emission is comparable to and perhaps balances the rate of Ohmic dissipation; this implies that the vacuum photodiode signals, in the absence of other emissive phenomena, are determined by the plasma resistivity and the instantaneous value of the current. Further support for this hypothesis is found by varying the discharge voltage of the main bank while holding the charging voltage of the fast gas valve capacitor bank fixed, for both the UV and optical emission are seen to be functions of the instantaneous value of the current. However, we note that the vacuum photodiode signals typically contain more structure than the optical photodiode signals, as is suggested in Fig. 4.1, and we believe that the vacuum photodiodes are sensitive to a broader range of phenomena than Ohmic dissipation of the main plasma current, as will be discussed further in Sec. 4.2.2.

4.1.3 Hydrogen Line Emission

The vacuum photodiode signals are quite large, but the mechanism responsible for producing such copious amounts of UV radiation has not yet been identified. Here, we present evidence that a significant portion of this UV radiation is hydrogen line emission. At first glance, this may seem obvious; since the plasma are composed of hydrogen, hydrogen emission should be significant. However, hydrogen line emission is typically not a significant source of radiation when the plasma is fully ionized, and analytical calculations of an equilibrium hydrogen plasma predict relatively minute radiation levels. However, the Solar Loop Experiment is fast and has magnetic field lines that link the electrodes; these factors keep the plasma out of equilibrium and increase its emission, perhaps explaining the magnitude of the vacuum photodiode signals. Other candidates for the EUV emission, impurity lines and thermal bremsstrahlung, will be presented in Sec. 4.1.4.

Line emission refers to the process whereby a bound electron orbiting an atomic nucleus collides with a free electron or photon, is excited to a higher energy level, and then radiatively decays to a lower energy state. The rate at which bound electrons are excited increases with both the free electron density and temperature, but if the ionization rate is too large then the vast majority of bound electrons will be ionized, resulting in a reduction in line emission. Thus, at fixed electron density, line emission typically rises to a peak and then falls as a function of temperature: at lower temperatures there are many bound electrons but few exciting collisions and at higher temperatures there are few bound electrons. This rise and then fall in line emission as a plasma heats up is known as a radiation barrier because the energy lost to line emission can balance Ohmic heating and prevent the plasma temperature from rising. If the Ohmic heating is sufficiently strong, though, the temperature will rise high enough such that radiation losses decrease; such a plasma is said to have "burnt through" the radiation barrier. Hydrogen presents a low-temperature radiation barrier of 1 - 2 eV [77, pg. 202] that is usually overcome in experiments, and the significant radiation barriers for a hydrogen plasma typically come from impurities [27, 78]. Indeed, the temperature of the Caltech plasmas is estimated at $2-3$ eV based on the ionization states of argon and nitrogen plasmas and based on the ionization states of carbon and oxygen impurities; as we shall soon see, such temperatures would suggest a nearly fully ionized plasma and very low hydrogen line emission.

The chief indication that hydrogen line emission is significant in the Solar Loop Experiment is that hydrogen line emission in the optical range is readily observed. By placing an H_α or H_β optical bandpass filter in front of the fast camera, it is seen that a significant fraction of the optical signal is due to H_α and H_β line emission. We can quantify the amount of power emitted in H_α and H_β by placing the same optical filters in front of the photodiode mentioned in Sec. 4.1. By applying conversion factors similar to those used in Eq. (4.9), including the 0.45 peak transmission coefficient of the optical filters, we obtain the H_α and H_β power traces plotted in Fig. 4.1 for a single loop hydrogen plasma formed with a 5 kV discharge with the fast gas valve capacitor bank charged to 500 V (shots 8987 and 8992). We shall show below that the power levels in these two optical lines alone exceeds the *total* power radiated as predicted by equilibrium models. Moreover, we note that the optical line intensities are strongly correlated with the vacuum photodiode signals and *increase* with time. This is significant because the current and hence Ohmic dissipation is likewise increasing in time, so the plasma temperature must be increasing until the radiative losses again balance the Ohmic dissipation. If during this process the plasma was close to equilibrium and the hydrogen was nearly fully ionized, then we would expect the hydrogen emission to *decrease*, or at least not increase, as the temperature rises even further beyond the radiation barrier. For example, on the Macrotor tokamak, the H_β signal peaks after 1 ms and then falls to a low value as the vacuum photodiode signals and oxygen line intensities continue to increase [48]. The behavior from Macrotor is indicative of full hydrogen ionization, or hydrogen burnthrough, while the optical-photodiode data from the Caltech Loop Experiment indicate that the hydrogen is still ionizing. Since weak hydrogen emission is due to full ionization of the hydrogen population, incomplete ionization would allow for strong hydrogen emission. The strong correlation between the hydrogen optical intensity and the vacuum photodiode signals is consistent with (but certainly does not prove) the possibility that the vacuum photodiode signal is entirely due to hydrogen emission.

Furthermore, from the optical emission we can estimate a portion of the hydrogen EUV emission and show that it is a substantial fraction of the total EUV emission measured by the vacuum photodiodes. The H_α line results from electron transitions from the $n = 3$ to $n = 2$ state; the rate of this transition is given by the transition probability per unit time $A_{32} = 4.4 \cdot 10^7\ \mathrm{s}^{-1}$ [79, pgs. 275 and 281] so that $N_{32} = A_{32} N_3$, where N_{32} is the number of H_α photons produced per second and N_3 is the number of hydrogen atoms in the $n = 3$ state. Knowing the H_α power level and that each H_α photons contains 1.89 eV, we estimate N_3:

$$N_3 = \frac{P_\alpha}{1.89\ \mathrm{eV}\ \cdot A_{32}}. \tag{4.10}$$

The Lyman β ($H_{\mathrm{L}\beta}$) line results from transitions from the $n = 3$ state to the $n = 1$ state, which occur at a rate $A_{31} = 5.6 \cdot 10^7\ \mathrm{s}^{-1}$. Since each $H_{\mathrm{L}\beta}$ photon contains 12.1 eV of energy, it follows that the power emitted in $H_{\mathrm{L}\beta}$ relative to the H_α power is

$$P_{\mathrm{L}\beta} = A_{31} N_3 \cdot (12.1\ \mathrm{eV}) = 8.15 \cdot P_\alpha. \tag{4.11}$$

A similar calculation relates the power of the Lyman γ line ($n = 4$ to $n = 1$) to the power from the Balmer β line: $P_{\mathrm{L}\gamma} = 7.74 \cdot P_\beta$. Using these calculations, we compute the $H_{\mathrm{L}\beta}$ and $H_{\mathrm{L}\gamma}$ contributions to the EUV emission and plot the result in Fig. 4.1. This calculated emission rises to 300 kW, about 10% of the peak EUV power of 3 MW. However, we have not accounted for the most powerful hydrogen line, the $H_{\mathrm{L}\alpha}$ line. Under the assumption of local thermodynamic equilibrium (LTE), to be discussed below, the power of the $H_{\mathrm{L}\alpha}$ would be about five times that of the $H_{\mathrm{L}\beta}$ line [80], in which case the powers of the $H_{\mathrm{L}\alpha}$, $H_{\mathrm{L}\beta}$, and $H_{\mathrm{L}\gamma}$ lines total to about one third of the total EUV emission. Clearly, the hydrogen emission is significant. Moreover, the LTE assumption, which is not expected to hold rigorously for the Caltech experiments, populates states according to the Saha-Boltzmann distribution, which favor the population of high n states. In Fig. 3 of Ref. [81], which describes plasma conditions very close to those of the Caltech Solar Loop Experiment, the low n states may have a higher population than that predicted by LTE, so the total hydrogen contribution to EUV emission might be even larger than one third. The current data is insufficient to determine exactly what percentage of the total power radiated comes hydrogen, and an experiment will be described in the next section to answer this question, but the optical photodiode data suggests that a substantial fraction of the EUV signal is hydrogen emission.

We now show that a pure hydrogen plasma in ionization equilibrium does not emit nearly as intensely as the Caltech Solar Loop Experiment. The intensity of line emission is determined by the populations of the associated ionization and excited states. These populations are in turn determined by a detailed balance of atomic processes, including collisional excitation and de-excitation as well as radiative de-excitation [82, 77]. The population levels are typically calculated numerically and can vary greatly based on the electron temperature and density. The temperatures and densities of the Caltech plasmas happen to be similar to the divertor region in a tokamak, for which effective average cross-sections for ionization and recombination that include multi-step ionization have been calculated [83] and are reproduced in Fig. 4.3. These cross-sections are *effective* because they include all excited states of neutral hydrogen; their utility, as explained by Stangeby, is that “one can proceed as if all the atoms were in the ground state” [84, pg. 138]. Thus, the effective ionization rate $\langle\sigma\nu\rangle_{\text{iz}}$ gives the rate of neutral hydrogen atoms, including all excited states, being ionized, and the effective recombination rate $\langle\sigma\nu\rangle_{\text{re}}$ gives the rate at which an electron and proton recombine to form neutral hydrogen of all excited states. The continuity equation for proton density n_i is then

$$\frac{\partial n_i}{\partial t} + \nabla \cdot (n_i \mathbf{v}) = \langle\sigma\nu\rangle_{\text{iz}}\, n_e n_0 - \langle\sigma\nu\rangle_{\text{rc}}\, n_e n_i, \tag{4.12}$$

where n_0 is the neutral hydrogen density, which includes all excited states. In Eq. (4.12), ionization acts as a source for protons whereas recombination acts as a sink. For this calculation, we assume a steady-state and homogenous plasma and set the lefthand side of Eq. (4.12) to zero. This is a poor assumption as the Caltech experiment is very fast (and thus not steady-state) and also has strong flows from the footpoints (implying strong convection), but by making such assumptions we will demonstrate the need for a non-equilibrium process to explain the strong energy discrepancy. The resulting ionization balance from setting the lefthand side of Eq. (4.12) to zero is

$$\frac{n_0}{n_i} = \frac{\langle\sigma\nu\rangle_{\text{rc}}}{\langle\sigma\nu\rangle_{\text{iz}}}. \tag{4.13}$$

We take the electron density to be $n_e = 10^{21}$ m^{-3}, based on Stark broadening of the H$_\beta$ line as discussed in Sec. 2.2.4, and $T_e \sim 2 - 3$ eV, based on the observed ionization states in nitrogen and argon plasmas and estimates from spectral lines of oxygen and carbon impurities. Using Fig. 4.3 at $T = 3$ eV, $\langle\sigma\nu\rangle_{\text{iz}} = 2 \cdot 10^{-9}$ cm^3/s and $\langle\sigma\nu\rangle_{\text{re}} = 4 \cdot 10^{-13}$ cm^3/s, which gives $n_0/n_i = 2 \cdot 10^{-4}$. At $T = 2$ eV, $\langle\sigma\nu\rangle_{\text{iz}} = 4 \cdot 10^{-10}$ cm^3/s and $\langle\sigma\nu\rangle_{\text{re}} = 9 \cdot 10^{-13}$ cm^3/s, which gives $n_0/n_i = 2 \cdot 10^{-3}$. In either case, the vast majority of hydrogen is ionized, and only the small fraction of remaining neutrals can participate in line emission.

To obtain the power radiated by such a hydrogen plasma, we utilize a second quantity called the emissivity, L. This quantity is related to the power radiated by $P_{\text{rad}} = L n_e n_0 \text{vol}$, where vol is the volume of the plasma. This quantity is computed numerically in Ref. [83] and is reproduced in Fig. 4.4. For a plasma with $n_e = 10^{21}$ m^{-3} and $T = 3$ eV, $L \approx 1.1 \cdot 10^{-20}$ ergs cm^3 s^{-1}, and $P_{\text{rad}} = \left(0.2 \text{ W/cm}^3\right) \cdot \text{vol}$. We estimate the plasma volume using the plasma dimensions given in Sec. 4.1.2, namely, a loop length of 20 cm and a radius of 2 cm, giving a volume of $\text{vol} = \pi r^2 l \approx 250$ cm^3. The total power is then only 50 W, a far cry from the megawatts estimated in the UV range and even from the optical power estimated from the photodiode. For $T = 2$ eV, we have $L \approx 6.5 \cdot 10^{-21}$ ergs cm^3 s^{-1}, and $P_{\rm rad} = 400$ W, which is again too small.

Another theoretical estimate of the plasma radiation can be done assuming local thermodynamic equilibrium (LTE). The LTE model assumes that the population levels are balanced by collisional excitations and de-excitations so that the excited states assume a Saha-Boltzmann distribution [77, pg. 118]. The calculations, performed by Vernon Chaplin, predict radiation levels that are somewhat higher than the ones derived above but that are still too low to account for the experimental observations. Even within the uncertainty used in estimating the plasma parameters, the theoretical emission from an equilibrium plasma appears too low to explain the experimental observations.

The large radiation levels suggest that the Caltech plasmas contain more neutrals than suggested by Eq. (4.13). High neutral densities are often associated with a lower-temperature plasma that is only partially ionized. Indeed, equilibrium hydrogen plasmas are typically most emissive when the electron temperature is such that the concentrations of ions and neutrals are about equal [77, pg. 202]. At 1 eV, $\langle\sigma\nu\rangle_{\rm iz} = 1.5 \cdot 10^{-12}$ cm^3/s and $\langle\sigma\nu\rangle_{\rm re} = 6.0 \cdot 10^{-12}$ cm^3/s from Fig. 4.3, which together with $L = 9 \cdot 10^{-22}$ ergs cm^3 s^{-1} and a plasma volume of 250 cm^3 predict an emission of 90 kW, which is significantly closer to the radiation losses observed experimentally. The temperature of hydrogen plasmas on the Caltech Solar Loop Experiment have not yet been accurately diagnosed, so our hydrogen plasmas may be slightly cooler than expected. However, C III (e.g., carbon ions with two electrons stripped) lines have been observed, which suggests an electron temperature greater than 2 eV [80][3]. However, we shall now see that non-equilibrium effects can allow a hydrogen plasma to radiate like a lower-temperature and partially ionized plasma even when the electron temperature suggests burnthrough.

The above calculations involve several assumptions that are quite dubious, and questioning these assumptions may help to explain the large vacuum photodiode signals. First, we assumed that the plasma is in equilibrium, but the duration of the Caltech Solar Experiment is not much longer than the ionization equilibration time for hydrogen atoms in the plasma conditions described. This equilibration time is roughly the time needed to ionize neutral hydrogen atoms injected into the plasma and is computed as follows. The analog of Eq. (4.12) for neutral hydrogen is

$$\frac{\partial n_0}{\partial t} + \nabla \cdot (n_0 \mathbf{v}) = -\langle\sigma\nu\rangle_{\rm iz} n_e n_0 + \langle\sigma\nu\rangle_{\rm rc} n_e n_i. \tag{4.14}$$

We ignore convection by setting $\mathbf{v} = 0$. Let the equilibrium densities be $n_{i,eq}$ and $n_{0,eq}$. If we then add a extra amount of neutral atoms, i.e. $n_0 = n_{0,eq} + \delta n_0$, then the continuity equation becomes

$$\frac{\partial(\delta n_0)}{\partial t} = -\langle\sigma\nu\rangle_{\rm iz} n_e (\delta n_0), \tag{4.15}$$

---

[3] This statement is based on the LTE assumption. While LTE may not be accurate for the Caltech experiments, we believe that it provides a rough estimate. In this case, at temperatures below 2 eV, carbon ions are predicted to be almost exclusiively in the C II ionization state.

from which the relaxation time τ is $\tau = 1/(\langle\sigma\nu\rangle_{\mathrm{iz}}\, n_e)$. At $T = 3$ eV and $n_e = 10^{15}$ cm^{-3}, we have $\tau \approx 0.5$ μs, and at $T = 2$ eV we have $\tau \approx 2.5$ μs. This relaxation time is not much shorter than the time scale of the plasma itself, so we cannot expect the plasma to be in equilibrium. This essentially means that the hydrogen does not have enough time to achieve the ionization balance predicted by Eq. (4.13) and that we can expect a larger number of neutrals. This proposed situation is similar to that investigated by Carolan and Piotrowicz, who studied the emission of impurities that have had insufficient time to achieve coronal equilibrium [85]. They found that impurities such as carbon and oxygen radiate more intensely at temperatures above burnthrough when not given enough time to equilibrate. We propose that hydrogen, the majority species, is behaving similarly: even though the temperatures of the Solar Loop Experiment may exceed burnthrough, the plasma may still radiate at very high levels as the neutrals gradually ionize over the course of microseconds. Note also that L, the emissivity, is two orders of magnitude higher at 3 eV than at 1 eV. Thus, it may be that the Solar Loop Experiment, because of its fast timescale, has a large population of neutrals like a lower-temperature, partially ionized plasma but, at the same time, has a larger value of L due to its higher electron temperature.

We also ignored convection in Eq. (4.13), but the Caltech Solar Loop Experiment certainly exhibits strong flows from the footpoints [43, 17]. It is generally accepted that plasma interaction with the chamber wall results in a larger density of neutral atoms as ions recombine with electrons from the wall. It is possible that this higher concentration of neutrals is then pumped out of the gas inlet via the MHD mechanism described in Sec. 2.1.5. Away from the wall, the neutrals would ionize on a microsecond timescale, during which time they would radiate far more intensely than an equilibrium plasma. Moreover, as suggested by Post, the presence of molecular hydrogen could increase the recombination rate by up to four orders of magnitude [83]! The molecular hydrogen concentration is expected to be very minute in the plasma itself but could be significant in the gas inlet.

In summary, a substantial fraction of the vacuum photodiode signals is hydrogen line emission, but the magnitude of such emission cannot be explained by emission from an equilibrium plasma. However, *non-equilibrium* effects might cause the plasma to radiate more intensely due to a large number of neutral atoms; the enhanced neutral concentration might be attributed to the short time scale of the experiment as well as the MHD pumping force that drives strong plasma flows from the wall. Given the uncertainties in the calculation, it is even conceivable that the vacuum photodiode signals are entirely caused by hydrgeon line emission; this hypothesis is supported by the correlation between the vacuum photodiode signals and the hydrogen optical line intensity. Of course, there are other sources of EUV radiation; in the following section we shall look into both impurity radiation and thermal bremsstrahlung and discuss their potential contributions to the vacuum photodiode signals.

4.1.4 Other Emission Processes

We now discuss two other radiation mechanisms: line emission from plasma impurities and thermal bremsstrahlung. Impurity line emission typically dominates the radiative losses of a hydrogen plasma, and one might suspect that the large vacuum photodiode signals are due to impurity emission. However, the previous section demonstrated that hydrogen emission is a substantial fraction of the total radiation, and we discuss in this section why impurity emission may not be as dominant for the Caltech Solar Loop Experiment as it is for other experiments. We also outline a future experiment to determine the relative contributions of hydrogen and impurity emission. Thermal bremsstrahlung, in contrast, is far too weak to contribute significantly the observed radiation levels.

In previous laboratory hydrogen plasmas, impurity line emission typically dominated the radiative losses. The reason for this, as discussed in the previous section, is that the hydrogen atoms quickly ionize and cease line emission. Impurities, although low in concentration, continue to radiate until fully stripped of all bound electrons, which may not occur until very high temperatures have been achieved. Moreover, the line emission of certain impurity ionization states can be quite intense. Impurities are a major hindrance to tokamak start-up [78] and have thwarted previous spheromak experiments [27]. In light of these previous experiences with impurity radiation, one might suspect that the excessively large vacuum photodiode signals should be due to impurity emission and that the hydrogen emission is negligible, as suggested by the analytical calculations. However, we have seen in the previous section that hydrogen emission is a non-negligible fraction of the total emission, so the role of impurities in the Caltech experiments may be less significant than for other previous experiments. This is probably because these previous experiments are typically hotter (so that the impurities are more emissive), last longer (so that the hydrogen has time to ionize more fully), and involve more interactions with the chamber walls (so that more impurities are introduced into the plasma). Indeed, from Figs. 3(d) and 4(d) from Ref. [85], the burnthrough temperature for carbon is 9 eV, and the burnthrough temperature for oxygen is about 20 eV. Because the Caltech plasmas are colder than both of these burnthrough temperatures, the impurity emission from these species will not be as intense as it is for other experiments at higher temperatures.

If impurity emission dominates the hydrogen emission, then one would expect impurity lines to be readily observed with the spectrometer. On the contrary, while the H_β line is readily measured on the Caltech Solar Loop Experiment, locating impurity lines has been somewhat difficult. Impurity lines were finally observed on one of the final experimental runs before a shutdown for maintenance; these lines were located by assuming that the plasma was slightly cooler (2 eV) than previously expected (3-5 eV) and also by aiming the spectrometer directly at the gas inlets from which the impurities originate. A sample of the spectrometer data with identified impurity lines[4] is shown in

---

[4] This spectral window is particularly rich in impurity lines, and analysis of this window, which is beyond the scope of this thesis, is expected to yield very useful information concerning temperature and relative impurity concentrations.

Fig. 4.5.a, whereas Fig. 4.5.b shows the H_β line, whose magnitude far exceeds that of any impurity line. There are many factors that must be taken into account when comparing the intensities of these spectral lines. The impurity spectra were obtained on shot 9163, a co-helicity hydrogen plasma with the gas valve supply charged to 500 V, while the H_β spectrum was obtained from shot 9024, a counter-helicity hydrogen plasma also formed with the gas valve supply charged to 500 V. For the impurity spectra, the spectrometer was gated for the entire lifetime of the plasma, whereas the H_β spectrum was obtained by gating only over a microsecond. For the impurity spectra, the spectrometer was aimed at the gas inlets, the brightest portion of the plasma, whereas the H_β spectrum was acquired from a line of sight about ten centimeters away from the electrodes. Clearly, the spectra should be compared under identical conditions, but, if the H_β spectra was measured with the spectrometer gated for the entire plasma duration and pointed directly at the gas inlets, we would expect the H_β line to be even more intense than shown in Fig. 4.5.

If the radiative losses are due entirely to impurity emission, then the implied impurity concentrations are suspiciously large. Carbon and oxygen are the "usual suspects" for low-Z impurities; the emissivity of carbon at $T_e = 3$ eV is roughly 10^{-32} Wm^3, while that of oxygen at the same temperature is $2 \cdot 10^{-33}$ Wm^3 [85, 83]. Carbon is thus more emissive at these temperatures, so we ignore oxygen. If we assume that the entire radiative losses, up to 1 MW as predicted by the vacuum photodiodes, are due to carbon emission alone, then

$$P_{\mathrm{C}} = 1\ \mathrm{MW} = L_C n_e n_C \mathrm{vol}, \tag{4.16}$$

and using $n_e = 10^{21}$ m^3 and vol = 250 cm^{-3} we get

$$n_C = \frac{1\mathrm{MW}}{L n_e \mathrm{vol}} = 4 \cdot 10^{20}\ \mathrm{m}^{-3}. \tag{4.17}$$

This implies that the carbon concentration is 40 percent of the electron density, or that the carbon concentration is roughly equal to the hydrogen concentration. This does not seem realistic. In the Swarthmore Spheromak Experiment, the carbon concentration is estimated to be 2 percent of the hydrogen concentration, which is nominally $5 \cdot 10^{20}$ m^{-3} [47]. The Swarthmore vacuum chamber is baked out to reduce impurity levels, but the Swarthmore plasmas also interact with a much larger surface area, including the coaxial spheromak guns that create the plasma. On the PISCES-B experiment, the baseline carbon ion fraction is 0.2%, and active injection of methane raises this fraction to only 2% [86]. Thus, a 40% carbon fraction seems unreasonably high.[5] Before concluding

---

[5] A similar analysis for hydrogen, with $L = 10^{-33}$ W m^3 at $T_e = 3$ eV, would require $n_H = 4 \cdot 10^{21}$ m^{-3} to produce a megawatt of power. This would imply that the plasma is far from ionization equilibrium, which agrees with the rising optical hydrogen line intensities observed during a shot. The density of the neutral gas puff on the Spheromak Experiment is believed to be well below 10^{21} m^{-3} [46], but this density has not been measured on the Solar Loop Experiment. Since the Solar Loop Experiment uses different power supplies for the gas valves, and since the gas valves are quite sensitive to the power supply [87], the Solar Loop Experiment may have a different density of neutral gas

too much from Eq. (4.17), though, we note that the values of n_e and T_e are not precisely known, and n_C is inversely proportional to n_e and is a strong function of T_e. For instance, if $T_e = 2$ eV then the $L_C = 2 \cdot 10^{-33}$ W m^3, and the required carbon concentration is five times higher. The plasma parameters are not currently known to sufficient precision to constrain the impurity concentration, and it is quite possible that impurities are contributing substantially to the radiative losses.

An experiment has been designed to determine the contribution of the $\mathrm{H_{L\alpha}}$ line to the vacuum photodiode signal in isolation from other lines. A pair of vacuum photodiodes will be installed in the middle of the vacuum chamber, roughly in the same location as the x-ray diodes shown in Fig. 2.1. By adjusting the collimation, these vacuum photodiodes will view the entire plasma on the Solar Loop Experiment. A lithium fluoride window will be installed over one vacuum photodiode; lithium fluoride has a sharp cutoff in the VUV just above the $\mathrm{H_{L\alpha}}$ line and has roughly a 50% transmission the $\mathrm{H_{L\alpha}}$ line. Surveying the main lines from low-Z impurities, the LiF window should filter out all impurity lines in the EUV. Thus, if the filtered vacuum photodiode registers a very small signal compared to the unfiltered vacuum photodiode, then the $\mathrm{H_{L\alpha}}$ line is not contributing significantly to the EUV emission. If, however, the filtered signal is roughly half of the unfiltered signal, then the Solar Loop Experiment does indeed possess strong hydrogen line emission even though the electron temperature suggests nearly complete ionization of hydrogen.

Bremsstrahlung is a radiation mechanism that is important for high-temperature plasmas but is insignificant for the Caltech experiments. Bremsstrahlung is the radiation emitted by an accelerated charge; in a plasma, an electron is continually being accelerated by Coulomb collisions with each particles, and the plasma emits a continuous spectrum based on the particle distribution function. Bremsstrahlung radiation from a thermal plasma is given in cgs units as [79, pg. 160]

$$\epsilon_\nu^{ff} = \frac{dW}{dt dV d\nu} = \frac{2^5 \pi e^6}{3mc^3} \sqrt{\frac{2\pi}{3mk_BT}} Z^2 n_e n_i e^{-h\nu/k_BT} \bar{g}_{ff}. \tag{4.18}$$

$\bar{g}_{ff}$ is the velocity-averaged Gaunt factor and can be taken to be about one for this calculation. The energy spectrum dies off exponentially for photon energies above the plasma temperature. As the Caltech plasmas have a temperature $T \approx 3$ eV, most of the bremsstrahlung energy is concentrated above the wavelength $\lambda_{\text{thermal}} = ch/(k_BT) = 410$ nm; this makes bremsstrahlung an unlikely can-

---

than the Spheromak Experiment. We can roughly estimate the neutral gas density as follows. The neutral gas flows from the fast gas valves through teflon tubes of volume 19 cm^3 into the main vacuum chamber, which has a volume of 1.8 m^3. When the gas valves are puffed, the chamber pressure rises on the order of 1 mtorr, which corresponds to $8 \cdot 10^{19}$ gas particles let in by a single puff. Since these particles travel through four teflon tubes (one for each gas inlet), when the gas puff is just exiting the gas inlets and occupies the tube volume, the neutral density is roughly $1 \cdot 10^{24}$ m^{-3}. We assume that, once the neutral gas reaches the gas inlet, it expands in a cone of opening angle 45 ° and that the linear density scales inversely with the cone radius squared. Under these assumptions, the neutral gas density a distance 4 cm away from the gas inlet would be $4 \cdot 10^{21}$ m^{-3} since the radius of the teflon tube is about 0.26 cm. This suggests that the Solar Loop Experiment may indeed start at a relatively high neutral density as would be required by the vacuum photodiode data assuming the radiation is mostly hydrogen line emission. Of course, neutral gas density measurements should be made on the Solar Loop Experiment to corroborate these "back of the envelope" calculations. The author would like to thank Auna Moser for assistance in comparing these calculations to measurements made on the Spheromak Experiment.

didate for explaining the large EUV emission observed by the vacuum photodiodes. Moreover, the overall power emitted by bremsstrahlung is rather small; integrating Eq. (4.18) over all frequencies gives

$$\frac{dW}{dtdV} = \frac{2^5 \pi e^6}{3mc^3} \sqrt{\frac{2\pi}{3m}} Z^2 n_e n_i \frac{\sqrt{k_B T}}{h}, \tag{4.19}$$

again in cgs units. Using $Z = 1$, $n_e = n_i \sim 10^{21}$ m^{-3}, and $T \sim 3$ eV, Eq. (4.19) gives 0.026 W/cm^3. From a plasma of volume 250 cm^3 the power of bremsstrahlung radiation is $P_{\text{brem}} \sim 6.6$ W, which is far too small to account for the power levels estimated by the vacuum photodiodes. Thermal bremsstrahlung is typically more important for hot plasmas because it increases with temperature whereas line radiation decreases assuming the plasma has burned through the radiation barriers. For a colder plasma like the ones produced in the Caltech experiment, though, thermal bremsstrahlung is inconsequential.

4.2 Co- Vs. Counter-Helicity Merging

The original purpose of the vacuum photodiode array was to provide spatial resolution to the EUV emission of co- and counter-helicity hydrogen plasmas. In this function, the array has indeed detected enhanced emission from counter-helicity merging that can, in many instances, be correlated with spikes in the x-ray diode signals. In this section, we shall compare co- and counter-helicity hydrogen plasmas formed with a 6 kV discharge voltage and a 500 V charging voltage on the fast gas valve capacitor bank. We shall find that something quite dramatic occurs for the counter-helicity plasma around 2.7 μs. At this time, EUV emission rises sharply, x-ray spikes are observed, the upper legs of the plasma brighten and appear to interact with the chamber wall, and a noise pulse is observed in the electronics. These events are believed to be related to magnetic reconnection and do not occur for a co-helicity plasma formed under the same conditions. As we shall see in Sec. 4.3, these events can be tamed by increasing the charging voltage of the fast gas valve capacitor bank, which admits more neutral gas into the chamber prior to breakdown.

For all counter-helicity shots presented in this section and in Sec. 4.3, the bias magnetic field was created in the RL configuration discussed in Sec. 2.1.3. The second configuration of the bias field that produces counter-helicity loops, LR, produces markedly different plasma behavior, as is discussed in Sec. 4.4. Such a dramatic difference in behavior is not observed between the two co-helicity configurations, and we will not distinguish between these two.

4.2.1 Comparing Co- and Counter-Helicity Plasmas

Fig. 4.6 overlays the vacuum photodiode signals for both a co-helicity shot (shot 7774) and a counter-helicity shot (shot 7763). All twelve channels of the array are plotted with the vertical channels plotted on the left column and the horizontal on the right. The upper left corner of each plot contains a legend to identify the position of the individual detector within the array. The emission from the two plasmas is remarkably similar for the first several microseconds, suggesting that co- and counter-helicity configurations have the same emission during this time and that this part of the vacuum photodiode signals is highly reproducible. Between 1.7 and 2.7 μs, however, the counter-helicity signal rises, sometimes precipitously, above the co-helicity signal. We hypothesize that this time is the beginning of the merging and that the large counter-helicity emission is due to the additional magnetic reconnection of the axial fields, as proposed in Ref. [20]. The mechanisms by which magnetic reconnection can cause enhanced radiation will be discussed in Sec. 4.2.2. The plots in Fig. 4.6 end at 4.7 μs; beyond this time, the vacuum photodiode signals vary significantly, and the signal levels can be quite high. We will not focus on these later signals as they do not correspond with the main plasma activity: the formation and growth of the plasma loop.

For counter-helicity plasmas, the large UV signals obtained from the topmost channels on the array are corroborated by fast camera images such as Fig. 4.7. Around the time of the UV burst, an intense brightness appears in the upper legs of the plasma, in the vicinity of channels 1 and 2 of the vacuum photodiode array, as the plasma loops merge and detach from the electrodes. This merging is seen more clearly in Fig. 4.9, in which the interframe timing of the Imacon fast camera is reduced to focus on this time period. Interactions with a bolt in the chamber wall several centimeters above the electrodes can occasionally be seen; the bolt is shown most clearly in Fig. 2.2. It is possible that the UV and x-ray signals originate from this interaction with the chamber wall. However, the UV burst typically persists for some time, up to a microsecond, while the arcing to the bolt dies down more quickly. Such intense activity is not seen in images of a co-helicity plasma, as shown in Fig. 4.8.

The rapid rise in the vacuum photodiode for counter-helicity plasmas is sometimes coincident with x-ray bursts on the x-ray diodes. Fig. 4.10 plots two such occurrences. The x-ray bursts that are plotted were obtained through the 200 nm thick Al foil filter whose transmission curve is plotted in Fig. 2.9; since this filter does not transmit hydrogen lines, the x-ray bursts, and perhaps part of the vacuum photodiode signals, must be caused by something other than hydrogen line emission. Different possibilities, such as bremsstrahlung from energetic electrons, are discussed in Sec. 4.2.2. We also note that the x-ray bursts presented here rise more sharply and at a slightly later time than the EUV bursts; this fact may be useful in determining the nature of the x-ray bursts.

The correlation between the x-ray diode data and the vacuum photodiodes data is not perfect; there are times when the x-ray diodes register a peak while no special activity is seen on the vacuum photodiodes, and vice versa. This lack of consistent correlation may be due to the sensitivity of the x-ray diodes to their alignment as discussed in Sec. 2.2.3. In fact, during the set of shots in which Fig. 4.10 was obtained, no significant x-ray activity was seen before 4.7 μs for the first several shots. Based on the large UV emission observed on the upper channels of the array, the x-ray diodes were re-aligned to point slightly upwards, after which x-ray bursts were seen on two of the next four shots. This anecdote demonstrates how sensitive the x-ray diode signals are to alignment and how the vacuum photodiode data can aid in aligning the x-ray diodes to optimize the chance of registering an x-ray burst. To improve the x-ray diode setup, a mechanical system should be implemented to precisely align the x-ray diodes in a reproducible fashion, or the collimation of the diodes should be redone in order to give the diodes a wide-angle view that covers the entire plasma.

Other differences between co- and counter-helicity plasmas can be seen in the plasma current and electrode voltage. Fig. 4.11 shows the plasma current and electrode voltage for both a co- and counter-helicity shot. The vertical dashed line is at 2.4 μs. At this time, the counter-helicity current begins to oscillate and fails to rise as rapidly as the co-helicity current. The oscillations are due to ringing in the electronics of the Rogowski coil and do not represent true current oscillations; they are similar to the oscillations that are induced by breakdown and that are seen at the beginning of the shot for both co- and counter-helicity plasmas. The deviance of the mean counter-helicity current, obtained by a boxcar average over 0.8 μs, from the co-helicity mean current may indicate that the reconnection process disrupts the current flow and that the plasma has trouble in re-establishing a current path. The primary motion of particles within a magnetized plasma is along magnetic field lines. As the bias field links the anode and cathode, the initial flow of current can be along these field lines. The reconnection process for counter-helicity plasmas, however, rearranges the field lines so that lines initially linking the anode and cathode now link the two quadrants of the anode and the two quadrants of the cathode. Electrons cannot flow along such field lines and contribute to the main current without drifting across such field lines.

The electrode voltages for both co- and counter-helicity shots are initially very similar. At 2.4 μs, both voltages drop, but the counter-helicity electrode voltage drops more sharply and afterwards has several rises and falls while the co-helicity trace progress more steadily to zero. As discussed in Sec. 2.2.2, a larger voltage may be associated with a rapidly expanding plasma, and a sudden drop in the electrode voltage may signify the change of the current to a shorter and lower-inductance path. The voltage drop at 2.4 μs might be similar to the voltage drop that occurs at breakdown. Also, a voltage spike can be interpreted in analogy to the spark that occurs when one unplugs an electrical appliance. In any electrical circuit carrying a current, if the circuit is suddenly opened, a large voltage will appear across the gap. This voltage spike is an attempt by the circuit to maintain the current flow. When unplugging toasters, the large voltage spike can result in a spark that allows current to continue flowing. The spikes that appear on the electrode voltage might be the analogous voltage spike as the loops detach and disrupt the flow of current. Regardless of the exact interpretation of the voltage signals, something drastic is occurring in a counter-helicity plasma after 2.4 μs but not in co-helicity plasmas.

4.2.2 Magnetic Reconnection, Current Sheets, and Energetic Electrons

Comparisons of the vacuum photodiode signals between co- and counter-helicity suggest that the signals consists of two components. The first component is a broad and smooth signal with a duration of several microseconds, while the second component consists of faster bursts that rise sharply and last from a microsecond down to tens of nanoseconds. This second component appears mainly in counter-helicity shots. In Sec. 4.1, we hypothesized that the vacuum photodiode signal are proportional to the rate of Ohmic dissipation, but in counter-helicity shots the vacuum photodiode signals spike significantly while the current does not. It seems unlikely that the resistivity of a counter-helicity plasma suddenly becomes much greater than its co-helicity counterpart, and we believe that some other mechanism is creating the large UV bursts seen in counter-helicity shots. We now discuss the possible ways in which magnetic reconnection, seen in Fig. 4.9, could produce the enhanced emission.

Magnetic reconnection involves current sheets that could produce local Ohmic heating in excess of the heating produced by the main plasma current; this excess heat would then lead to larger radiative losses. Current sheets arise during magnetic reconnection because the merging magnetic fields induce an electric field that drives currents via Ohm's law [2, ch. 12]. In this way, the energy contained in the magnetic fields that are being annihilated can be transferred via Ohmic dissipation to the plasma particles, and, under the hypothesis of Sec. 4.1.2, the Ohmic heat generated inside the current sheet will be radiated away. We can estimate the plausibility of this argument by calculating the energy contained in the magnetic field and comparing it to the power radiated by the counter-helicity bursts in excess of the co-helicity signals. We use a typical magnetic field strength of $B \approx 0.1$ T. The volume of plasma within the view of a single vacuum photodiode is $\text{vol} = 2\pi r^2 \cdot l$; the factor of two comes from the fact that there are two loops, the loop radius r will be taken to be 0.02 m, and the length l will be the diameter of the vacuum photodiode's viewcone, calculated in Sec. 3.5.3 to be about 9.4 cm. With these values, the energy contained in the axial field is roughly 1 J; liberating this energy over the course of a microsecond would correspond to power levels of 1 MW. The observed difference between counter- and co-helicity radiation levels, estimated from channel 1 of the vacuum photodiode array data plotted in Fig. 4.6, is approximately 0.25 MW. Thus, it is not unreasonable to suggest that the counter-helicity EUV bursts are energized by the reconnection of the axial field.

Another radiation mechanism is bremsstrahlung from a small population of energetic, non-thermal electrons excited by magnetic reconnection. Such bremsstrahlung would be of a higher frequency and intensity that of the thermal electrons. Electrons may be energized by the induced electric field associated with magnetic reconnection; this has been observed in tokamaks [31, 32], the magnetosphere [88, 89], and in numerical simulations [28, 29]. One interesting feature of plasmas is that faster-moving particles experience fewer collisions, so populations of energized electrons may exist for some time before being thermalized by collisions. Energetic electrons might explain the bursts seen on the filtered x-ray diode, for the filter blocks all hydrogen lines as shown in Fig. 2.9. Therefore, the filtered x-ray diode signals must come from another mechanism, either energetic electrons or perhaps some impurity line that only begins to radiate during reconnection.

4.3 Counter-Helicity Behavior as a Function of Neutral Gas Levels

The above comparison between co- and counter-helicity experiments was conducted with the gas valve power supply charged to 500 V, for which a relatively spectacular event occurs in counter-helicity plasmas sometime between 1.7 and 2.7 μs. These spectacular events, however, can be diminished by increasing the charging voltage of the fast gas valve capacitor bank, which lets more neutral gas into the chamber before the shot. In general, counter-helicity plasmas formed with a higher charging voltage of the fast gas valve capacitor bank produce sharper fast camera images, emit less UV and x-ray radiation, expand and detach slower, and have smaller electrode voltage rises. These observations are consistent across counter-helicity plasmas made from hydrogen, nitrogen, and argon. Interestingly, though, while the overall EUV emission from a hydrogen plasma decreases as the charging voltage of the fast gas valve capacitor bank is changed from 500 V to 550 V, extremely large emission appears on the outer channels of the vacuum photodiode array; these bursts in UV are believed to originate from the central bright spots described in Ref. [20] and in Sec. 1.4.1.

Increasing the charging voltage of the fast gas valve capacitor bank creates a plasma of higher peak density. This is suggested in Table 2.1, which shows that the total amount of hydrogen puffed into the chamber rapidly rises with the charging voltage, but these measurements do not prove that the extra gas ends up as ionized plasma in the loops. However, electron density measurements confirm that the peak density of a counter-helicity hydrogen plasma formed with a 550 V charging voltage on the fast gas valve capacitor bank is indeed larger than that of a similar plasma formed with a 500 V charging voltage. The density is determined by measuring the Stark broadening of the H_β lines as described in Sec. 2.2.4. For these measurements, the spectrometer's channels were aligned horizontally so that the twelve spectrometer chords extend out along the midplane away from the electrodes, as shown in Fig. 4.12. The gate time of the spectrometer's CCD camera was set to a 1 μs time window, and this time window was systematically shifted to locate the time of peak density for each gas voltage setting. For a 500 V charging voltage of the fast gas valve capacitor bank, the average peak density was $n_e = (6.5 \pm 1.0) \cdot 10^{20}\ \mathrm{m}^{-3}$ obtained by gating from 2 to 3 μs. For a 550 V charging voltage, the average peak density was $n_e = (12.2 \pm 2.3) \cdot 10^{20}\ \mathrm{m}^{-3}$ obtained by gating from 3 to 4 μs . Figure 4.12 plots the density profiles at these times. Note that the plasma does not become less dense after this time but rather drifts past the spectrometer field of view; more work should be done to investigate the densities at later times. The peak density values reported here are obtained by first averaging over several shots and then averaging the three channels with the largest density values. The error bars in fig. 4.12 represent the shot-to-shot variations. The ratio of peak density is 1.88 ± 0.47. These measurements are rough and can be improved by refining the experimental techniques, but the preliminary results indicate that the plasma does indeed become denser when the charging voltage of the gas supply is increased.

For the remainder of this section, we shall use the following nomenclature. Plasmas formed with the fast gas valve capacitor bank charged to 500 V will be referred to as low-mass plasmas, plasmas formed with the fast gas valve capacitor bank charged to 550 V will be referred to as mid-mass plasmas, and plasmas formed with the fast gas valve capacitor bank charged to 600 V will be referred to as high-mass plasmas. Obviously, the words “low,” “mid,” and “high” are relative and perhaps subjective, but this naming scheme is more concise than specifying the value of the charging voltage on the fast gas valve capacitor bank for each plasma.

Fast camera images show that increasing the charging voltage of the fast gas valve capacitor bank produces sharper images, slows the expansion of the loops, and delays detachment from the electrodes. Fig. 4.13 shows a sequence of images for a mid-mass plasma (shot 7982); it is sharper than its low-mass counterpart shown in Fig. 4.7. We also note that both the lower and upper legs of the mid-mass plasma become bright, in contrast to the low-mass plasma. Fig. 4.14 superimposes both Fig. 4.7, colored green, and Fig. 4.13, colored blue. This superposition clearly demonstrates that the mid-mass plasma expands slower than its low-mass counterpart. This is not surprising, as the mid-mass plasma was shown by spectroscopic measurements to be denser and is thus accelerated less by the magnetic forces than the low-mass plasma. Since the mid-mass plasma expands more slowly, its footpoints detach from the electrodes at a later time than the low-mass plasma; in Fig. 4.14, the low-mass plasma appears detached at frame 7, or 2.30 μs, but the mid-mass plasma does not detach until frame 10, or 3.35 μs.

The two different charging voltages of the fast gas valve capacitor bank produce different levels of EUV emission as well. Fig. 4.15 overlays the vacuum photodiode signals for a low-mass plasma (shot 7755) with that of a mid-mass plasma (shot 7980). For the low-mass plasma, the strongest emission comes from the very top of the plasma with strong emission propagating down the inner channels, which are plotted in the lefthand column. The signals from the upper channels are not as intense in the mid-mass plasma, but channel 11 registers enormous radiation that seems isolated to the outermost channels. [6] Such large yet localized radiation is not seen on the outer channels for low-mass plasmas, and we hypothesize that this radiation is emanating from the bright central region. When the vacuum photodiode signals are summed over the entire array, the EUV emission from the low-mass plasma is comparable to or even larger than the mid-mass plasma for the first several

---

[6] The data presented in Fig. 4.15 shows an intense radiation burst only on channel 11 in the mid-mass plasma, but other shots with the same parameters show large emission from channel 10 as well.

microseconds. This is surprising, as plasma emission typically scales like the square of density, so denser plasma are expected to have higher radiation losses. The Caltech plasmas may be so dense that they have achieved the high-density limit of radiation losses observed in magnetic confinement devices [78].

Both the plasma current and voltage change appreciably in response to increasing the charging voltage of the fast gas valve capacitor bank. We focus first on the current. Increasing the charging voltage causes the plasma current to peak sooner and at a larger value as seen in Fig. 4.16, which plots the discharge currents for a low-mass, mid-mass, and high-mass plasma together (shots 8203, 8205, and 8208 respectively). The mean current, obtained by a boxcar averaging over 0.8 μs to remove the spurious oscillations, reaches a peak value of 65 kA for the low-mass plasma but reaches 85 kA for the mid-mass plasma and 90 kA for the high-mass plasma. We observed in Sec. 4.2.1 that the low-mass plasma current undergoes a disruption and deviates from the expected sinusoidal behavior; Fig. 4.16 shows that this disruption is less apparent for the mid-mass and high-mass plasmas. The current data also contains spurious oscillations on the Rogowski coil that appear at breakdown and again in the middle of the shot. These spurious oscillations are less severe for the mid-mass plasma and are almost entirely absent for the high-mass plasma.

Imacon images show that low-mass plasmas expand faster and detach sooner from the electrodes, and we hypothesize that this abrupt detachment may be responsible for disrupting the flow of current and inducing the oscillations. A mid-mass plasma expands at a slower pace and perhaps detaches in a smoother fashion, resulting in less disruptions and a steadier current. Imacon images for high-mass plasmas show that the plasma remains attached to the electrodes for a very long time, and indeed, the current trace for a high-mass plasma is the smoothest of all, peaking at more than 90 kA and suffering the least disruption around 2.7 μs.

Because the current traces obtained with a larger gas valve voltage return to zero at earlier times, one might attribute the change in current to the differences in plasma inductance due to the change in expansion rates. A rapidly expanding plasma quickly grows in size and has a larger inductance than a slowly expanding plasma. If we model the plasma and capacitor bank as an LRC circuit, then the current would have larger amplitude and shorter period with a smaller inductance. However, a close look at Fig. 4.16 shows that the mean values of the three currents are almost identical over the first microsecond even though the plasmas are expanding at different rates at this time. The difference in current appears to begin at a particular time, which seems more consistent with a change in magnetic topology that begins at the onset of reconnection rather than a difference in expansion rates, which is in action even at the beginning of the shot. Moreover, if the current finds a new path as the plasma detaches, then the size and inductance of the plasma loop will have little influence on the current profile after detachment. Really, to study this matter further, the path of the current should be determined before and after detachment. This may involve detailed measurements using the magnetic probe or perhaps the development and installation of small and moveable Rogowski coils inside the chamber.

More insight can be obtained from the voltage traces. Three voltage traces for a low-mass, a mid-mass, and a high-mass plasma (shots 8203, 8205, and 8208 respectively) are plotted together in Fig. 4.17. The traces are synchronized such that breakdown for all three shots occurs at 0.0 μs. The large signals prior to 0.0 μs are simply the main bank applying the discharge voltage to the electrodes before current can flow. For the low-mass plasma, the neutral gas takes more than a microsecond to breakdown; for mid-mass and high-mass plasmas the breakdown time is progressively shorter. For non-hydrogen plasmas, the breakdown time can be even longer. After breakdown, all three voltage traces drop to about 2 kV. However, the low-mass plasma voltage starts to rise significantly to 4 kV until, at about 2.7 μs, it plummets again. The voltage rise is presumed to be associated with the rapid expansion while the voltage plummet is associated detachment as the current finds an alternate, lower inductance path. We do not see this steady rise for mid-mass plasmas, but we do see a voltage spike at 2.7 μs. For high-mass plasmas, the voltage is more or less flat with a minimal rise at 2.7 μs. This trend of a flatter voltage trace with increased charging voltage of the fast gas valve capacitor bank is seen in both nitrogen and argon plasmas as well.

In summary, all of the disruptive features exhibited by counter-helicity plasmas that are absent in co-helicity plasmas can be mitigated by increasing the charging voltage of the fast gas valve capacitor bank, which admits more neutral gas into the chamber and produces denser plasmas. We hypothesize that these disruptive features are signatures of a change in magnetic topology and that this change is slowed down by increasing the plasma's density and hence inertia. Of course, this hypothesis needs to be verified by measurements of the magnetic field in the vicinity of the footpoints. Another intriguing possibility is that the plasma becomes "gas starved" for lower charging voltages. That is, the MHD pumping force described in Sec. 2.1.5 may exhaust the local density of plasma in the footpoints for lower charging voltages, leading to disruptive behavior. It may be possible to align the spectrometer in such a way as to measure the density in the gas inlet without simultaneously measuring the density of the plasma loop immediately outside the inlet. Such measurements would shed light on the nature of the plasma detachment.

4.4 Bias Field Configuration

In the course of these studies, an interesting observation has been made regarding the polarity of the bias magnetic field. This section documents this finding in the hopes that a future graduate student will someday explain this phenomena. As noted in Sec. 2.1.3, there are two field configurations that produce counter-helicity shots. In principle, these two configurations should produce plasmas that are mirror-images of each other. Experimentally, though, significant differences have been found between the two field configurations. The RL configuration produces bright spots and enhanced x-ray emission as has been discussed. The LR configuration, however, does not form bright spots and does not emit strongly in x-ray during the first several microseconds of the experiment. In fact, at times when the RL configuration becomes bright at the legs, the LR configuration becomes quite dim. However, at much later times, around 7.2 μs after breakdown, the LR configuration begins to arc brightly across the electrodes while a plume of plasma is seen to brighten, erupt, and detach. Fig. 4.18 shows an LR configuration formed with a 500 V charging voltage on the fast gas valve capacitor bank; this figure should be compared with Fig. 4.19, which has the same parameters and camera timings but a bias field configuration RL. It is not clear why reversing the magnetic field configuration should cause such a drastic change in plasma behavior, and this asymmetry should be investigated further. In particular, the delayed eruption of plasma may have implications for solar physics.

4.5 Conclusions and Directions for Future Work

This chapter presents two main conclusions regarding the vacuum photodiode signals. First, the signal amplitudes imply intense radiative losses from the plasma that appear consistent with the hypothesis that the plasma radiates away any heat deposited by Ohmic dissipation. Moreover, if this intensity is due to hydrogen line emission, then the plasma must be well out of equilibrium with an enhanced concentration of neutrals. Second, very intense emission is observed at the upper legs of a counter-helicity hydrogen plasma formed with a 500 V charging voltage on the fast gas valve capacitor bank. This burst coincides with localized brightness in camera images at the upper leg, interactions with a chamber bolt, oscillations on the current data, a peak and sharp drop in voltage, and occasional coincidences with x-ray bursts. This intense radiation burst is not observed for co-helicity plasmas and also seems to disappear as the gas voltage is increased. We believe it is related to the magnetic reconnection associated with counter-helicity merging.

The intense radiation from a non-equilibrium hydrogen plasma could be of use in divertor physics. There, radiation is a means by which the plasma temperature can be controlled so that the hot plasma from the core does not damage the diverter plates [83, 90, 81]. The Caltech Solar Loop Experiment suggests that cold plasma with an abnormally high neutral concentration can be magnetically pumped from the wall region into the divertor volume along arched field lines, inducing intense radiation and potentially quenching the local plasma temperature. The use of cold hydrogen plasma, rather than impurities, to induce radiative loss might be advantageous since the hydrogen will eventually ionize and cease radiation after a certain amount of time, whereas impurities will continue to radiate and might also “leak” into the plasma core. Intense hydrogen emission might also have the practical application of producing large amounts of EUV radiation for lithography.

We conclude with some comments concerning directions for future research.

- The most important avenue for future research is the determination of what, exactly, is generating the large vacuum photodiode signals for a hydrogen plasma. Section 4.1.4 discussed an experiment involving filtered vacuum photodiodes that will potentially answer this question. Because vacuum photodiodes are inexpensive and easy to construct, a filtered array could be constructed to greatly expand upon the spectal resolution of the EUV data. We note that a more direct, albeit involved and expensive, solution would be to install a vacuum ultraviolet spectrometer to directly observed the EUV lines most responsible for the radiative losses. The filtered vacuum photodiodes would certainly provide the preliminary knowledge needed to decide if a vacuum ultraviolet spectrometer is a worthwhile investment

- If the source of the large vacuum photodiode signals is indeed hydrogen line emission, then our hydrogen plasmas must be well out of equilibrium. The Caltech Spheromak Experiment can produce similar plasmas with extended current pulses. Therefore, performing similar experiments on the Spheromak Experiment could provide useful tests of the hypothesis proposed here.

- The usefulness of the x-ray diodes is currently limited by their sensitivity to alignment. The signals are collimated in part due to powerful neodymium magnets that protect the diodes against charged particles, just like the vacuum photodiodes. The magnetic deflecting system should be redesigned to increase the field of view so that the x-ray diodes can view the entire plasma, eliminating the sensitivity to alignment.

- Another crucial matter is determining where the current is flowing in the plasma. As mentioned, magnetic data on the Spheromak Experiment suggests that current flows in a channel several times larger than the visible plasma seen in Imacon images. If the same holds true for the Solar Loop Experiment, then calculations performed with a plasma radius determined from Imacon images will be misleading. Furthermore, if the plasma has truly detached from the electrodes, then current should not be flowing through the loop but through some other path. Determining how and when this occurs during a shot will greatly help in the interpretation of diagnostic data.

- The noise burst observed in counter-helicity experiments should be investigated further, as it may be indicative of plasma waves being generated during magnetic reconnection. This can be investigated by building a radiometer to detect plasma radiation in the radio-frequency range, the frequency range of the observed noise. One might also use the magnetic probe or a capacitively coupled probe to detect waves within the plasma.

- These studies have clearly identified the neutral gas density profile as a major factor in the plasma evolution. However, this profile has not been studied in detail on the Solar Experiment. A fast ion gauge should be constructed to map out the density of the neutral gas cloud at the time of breakdown and how this density changes as a function of the charging voltage of the fast gas valve capacitor bank.

- The asymmetry in the bias magnetic field should certainly be investigated further. In particular, this might give insight into why counter-helicity plasmas in the RL configuration has intense emission in the upper half but not the lower half.

- The role of arcing and the bright light from the gas inlet should be investigated. As the x-ray diodes point directly at the electrodes, it is possible that particle bombardment of the electrodes is producing x-rays observed by the x-ray diodes.

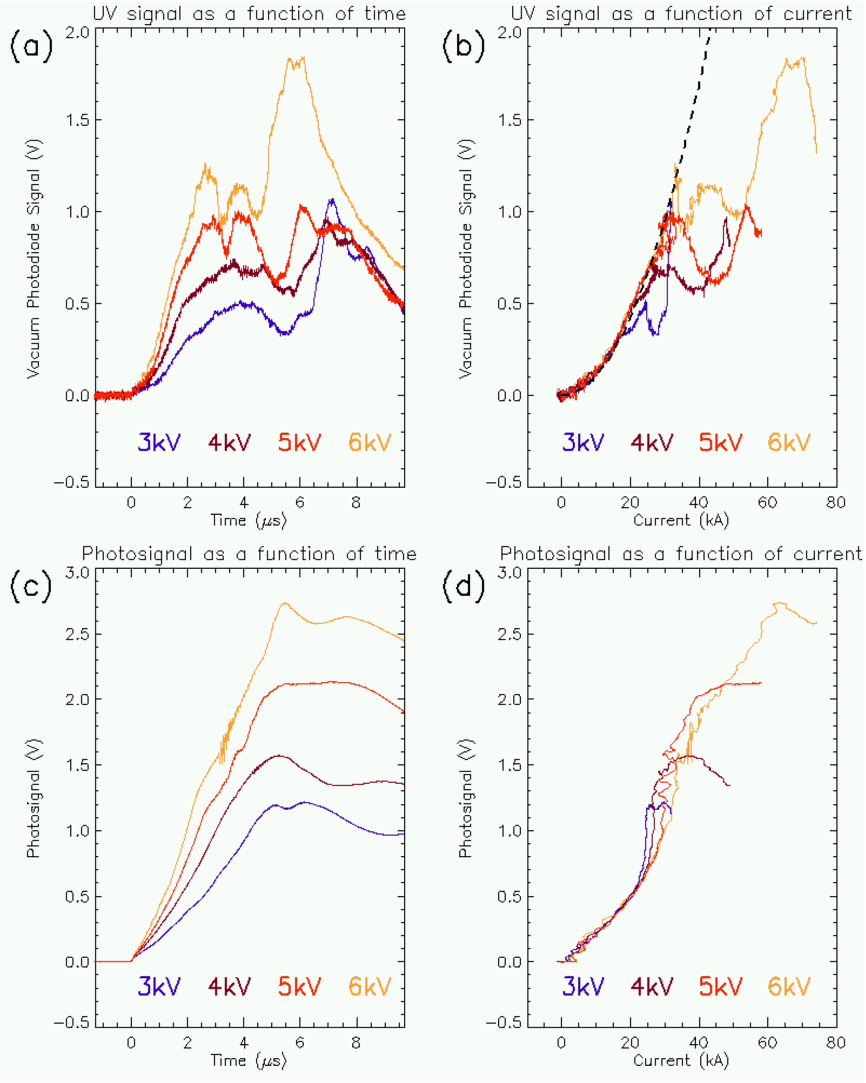

Figure 4.2: (a): Vacuum photodiode signals taken at various discharge voltages and plotted as a function of time. Larger discharge voltages produce faster rising vacuum photodiode signals. (b) The same data are now plotted as a function of current. The UV emission is seen to depend on the instantaneous value of the current. The thick dashed line is a quadratic fit, which yields a plasma resistance of 5.3 mΩ. (c) and (d) are analogous plots made for optical photodiode data; the same trends can be observed. The shots used for these plots were 8957 - 8960, which were single-loop hydrogen shots with the fast gas valve capacitor bank charged to 550 V.

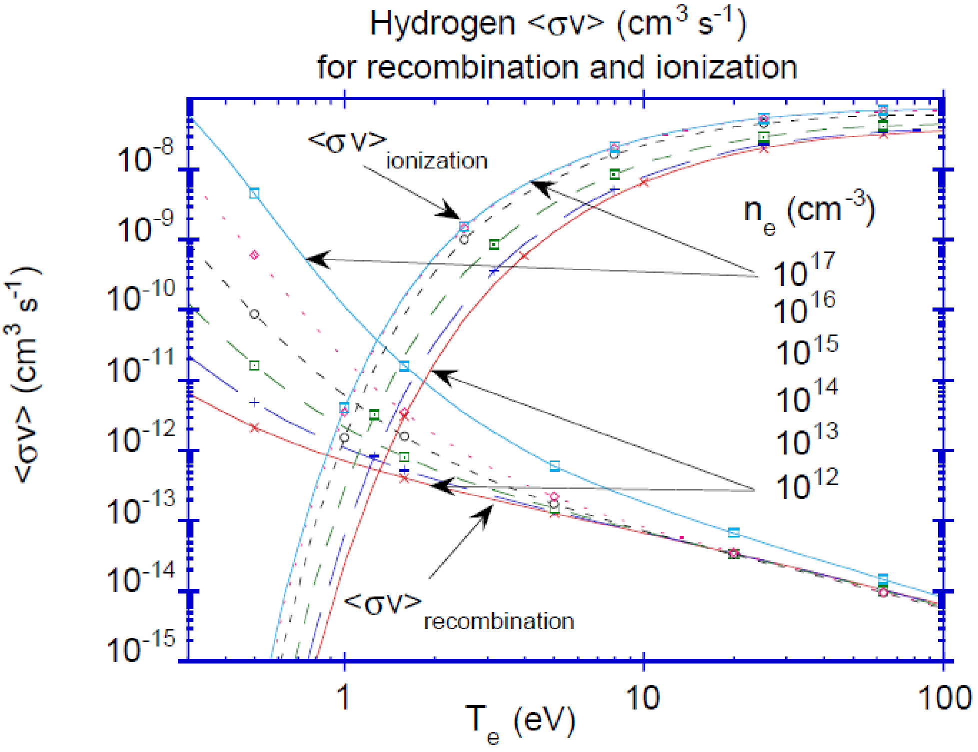

Figure 4.3: The effective ionization and recombination rates for hydrogen at different densities and temperatures, reproduced from Ref. [83]. The ratio of these two rates determines the equilibrium ionization balance and hence neutral hydrogen concentration.

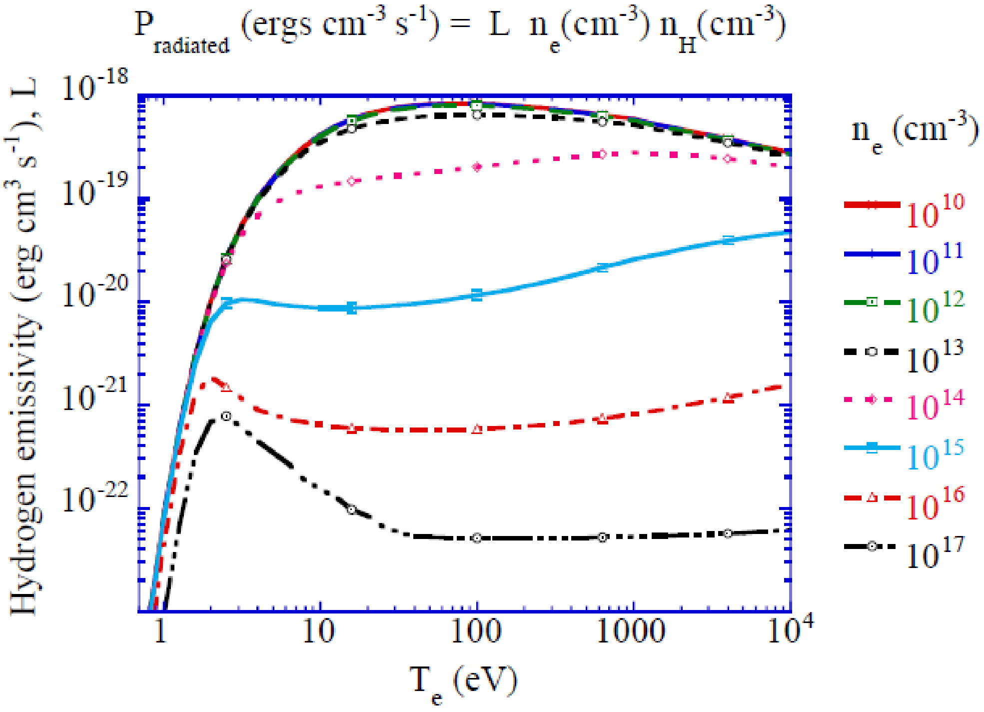

Figure 4.4: The radiation emissivity for hydrogen at different temperatures and densities, reproduced from Ref. [83]. This coefficient, when multiplied by the electron density, neutral density, and plasma volume, gives the radiation power.

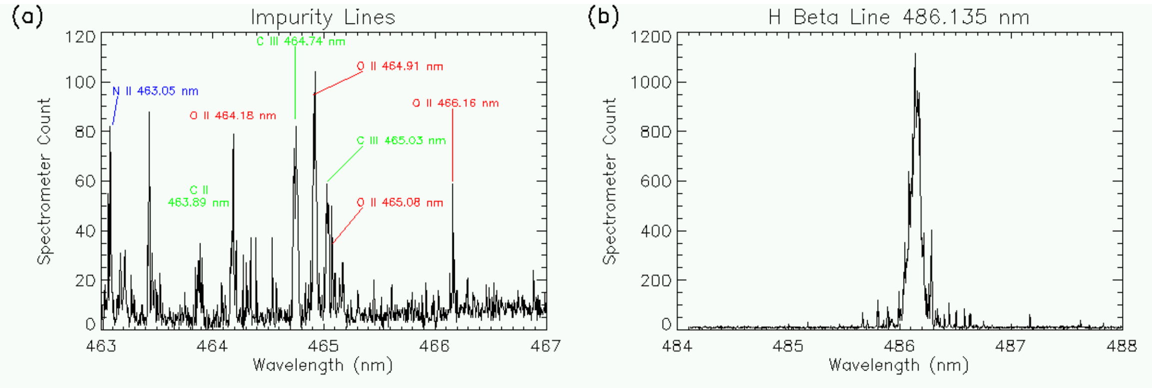

Figure 4.5: (a) A number of impurity lines have been observed in hydrogen plasmas. (b) The H_β line is noticeably stronger than the impurity lines.